ARL-TN-1133 ● SEP 2022

DEVCOM ARMY RESEARCH LABORATORY

X-ray Computed Tomography Evaluation and Analysis of Cast Aluminum Test Specimens Conducted Under the Army Research Laboratory's Advanced Manufacturing Co-Design Program

by William Green, Keaton Klaff, Charles Pergantis, and Taylor Cain

NOTICES

Disclaimers

The findings in this report are not to be construed as an official Department of the Army position unless so designated by other authorized documents.

Citation of manufacturer's or trade names does not constitute an official endorsement or approval of the use thereof.

Destroy this report when it is no longer needed. Do not return it to the originator.

ARL-TN-1133 ● SEP 2022

X-ray Computed Tomography Evaluation and Analysis of Cast Aluminum Test Specimens Conducted Under the Army Research Laboratory's Advanced Manufacturing Co-Design Program

William Green, Charles Pergantis, and Taylor Cain
DEVCOM Army Research Laboratory

Keaton Klaff
Bennett Aerospace

REPORT DOCUMENTATION PAGE

Form Approved
OMB No. 0704-0188

PLEASE DO NOT RETURN YOUR FORM TO THE ABOVE ADDRESS.

1. REPORT DATE *(DD-MM-YYYY)*	2. REPORT TYPE	3. DATES COVERED (From - To)
September 2022	Technical Note	31 March–29 June 2022

4. TITLE AND SUBTITLE

X-ray Computed Tomography Evaluation and Analysis of Cast Aluminum Test Specimens Conducted Under the Army Research Laboratory's Advanced Manufacturing Co-Design Program

5a. CONTRACT NUMBER

5b. GRANT NUMBER

5c. PROGRAM ELEMENT NUMBER

6. AUTHOR(S)

William Green, Keaton Klaff, Charles Pergantis, and Taylor Cain

5d. PROJECT NUMBER

5e. TASK NUMBER

5f. WORK UNIT NUMBER

7. PERFORMING ORGANIZATION NAME(S) AND ADDRESS(ES)

DEVCOM Army Research Laboratory
ATTN: FCDD-RLW-MB
Aberdeen Proving Ground, MD 21005

8. PERFORMING ORGANIZATION REPORT NUMBER

ARL-TN-1133

9. SPONSORING/MONITORING AGENCY NAME(S) AND ADDRESS(ES)

10. SPONSOR/MONITOR'S ACRONYM(S)

11. SPONSOR/MONITOR'S REPORT NUMBER(S)

12. DISTRIBUTION/AVAILABILITY STATEMENT

Approved for public release: distribution unlimited.

13. SUPPLEMENTARY NOTES

ORCID IDs: William Green, 0000-0001-8772-3946; Taylor Cain, 0000-0002-6621-914X

14. ABSTRACT

The objective of the US Army Combat Capabilities Development Command Army Research Laboratory's Advanced Manufacturing Co-Design Program is to exceed the traditional design paradigm in time and quality. The trade-off between quality of solution and time spent searching the immense design space dictates when and what solution is attainable. In traditional design, process optimization and part optimization are performed independently, ignoring the inherent dependence of materials and part properties on processing conditions. A main focus of the co-design program is to develop and test novel additive manufacturing (AM) and casting methods for near-net or net-shape production of aluminum metallic components. The co-design program builds AM thermoplastic polyester polylactic acid specimens or parts, which are then used to produce metallic specimens or components using a novel casting process. X-ray computed tomography scanning and evaluation was used to generate complete, closed-surface models of several cast metallic specimens, which were used to perform nominal-to-actual comparison analyses of production or desired surface models (i.e., STL files) to the surface geometries of their actual manufactured specimens.

15. SUBJECT TERMS

Sciences of Extreme Materials, X-ray computed tomography, XCT; nondestructive evaluation, NDE; additive manufacturing, AM; casting; aluminum, Al; star specimens, object-model comparison

16. SECURITY CLASSIFICATION OF:			17. LIMITATION OF ABSTRACT	18. NUMBER OF PAGES	19a. NAME OF RESPONSIBLE PERSON
a. REPORT	b. ABSTRACT	c. THIS PAGE			William Green
Unclassified	Unclassified	Unclassified	UU	29	19b. TELEPHONE NUMBER (Include area code) (410) 306-0817

Contents

List of Figures

List of Tables

1. Introduction

The X-ray computed tomography (XCT) technique is a widely applicable and powerful nondestructive inspection modality for evaluation and analysis of geometrical and physical characteristics of materials, especially internal structures and features. XCT is applicable to metals, ceramics, plastics/polymers, and composites, as well as components, assemblies, and materiel. The principal advantage of XCT is that it provides densitometric (i.e., radiological density and geometry) images of thin cross sections through an object in a noninvasive manner. Because of the absence of structural superimposition, images are much easier to interpret than conventional radiological images. The user can quickly learn to read XCT data because images correspond more closely to the way the human mind visualizes 3-D structures than 2-D projection radiology (i.e., film radiography, real-time radiography, and digital radiography).[1–4] The US Army Combat Capabilities Development Command Army Research Laboratory's Army Research Directorate (ARD) has identified additive manufacturing (AM) in general, and of certain materials and components in particular, as an essential research area. Work in polymers, ceramics, and metals AM to varying degrees is an applied research and development area of the ARD's Sciences of Extreme Materials Division.

The objective of the DEVCOM Army Research Laboratory's Advanced Manufacturing Co-Design Program is to exceed the traditional design paradigm in time and quality. The trade-off between quality of solution and time spent searching the immense design space dictates when and what solution is attainable. In traditional design, process optimization and part optimization are performed independently, ignoring the inherent dependence of materials and part properties on processing conditions. Such a design process excludes valuable (and often readily obtainable) information establishing relationships between design choices and output performance, leading to longer development cycles and suboptimal designs. Development and utilization of machine learning (ML) techniques and protocols to use dimensional comparisons of original designs to actual parts in a feedback loop to the processing system (or operator) is a future goal of the co-design program. The techniques would be used to attain dimensional consistency by quicker correction of deviations and thus produce higher quality parts.

The overall purpose of the ARL Advanced Manufacturing Co-Design Program is to develop and test novel AM and casting methods for near-net or net-shape production of aluminum (Al) metallic components. The co-design program builds AM thermoplastic polyester polylactic acid (PLA) specimens or parts, which are then used to produce metallic specimens or components using a novel casting

process. XCT is applicable to both steps in the production process providing both full 3-D characterization of the PLA "blank" as well as of the final metallic specimen or component. XCT scanning and evaluation was used to generate complete, closed surface models of several AM or cast metallic specimens, which were used to perform nominal-to-actual comparison analyses of production or desired surface models (i.e., STL files) to the surface geometries of their actual manufactured specimens.

2. Casting Process

ARL identified that the high manufacturing costs associated with traditional design and production of parts and components can be mitigated using AM. The co-design program aims to develop and apply novel AM and casting-related methods. First, a PLA version of the specimen is made using AM. Second, once the PLA blank was prepped, it was placed within a metal flask and encapsulated with investment casting plaster to fill the remaining volume within the flask. The flask was placed in a kiln and subjected to a specific heating profile, up to 700 °C to burn out and eliminate all the PLA material, thus leaving behind a cavity for the desired pattern to be cast. The mold (kiln) temperature was reduced to 500 °C for casting and metal liquid introduced into the vacant cavity. The metal was then allowed to cool, flask removed from the kiln, and plaster/metal separated from each other by quenching in water to reveal the finished bulk casting. The test specimen or specimens were then cut off, well cleaned, and legs color coded prior to XCT scanning to keep track of sample orientation and alignment. Castings were composed of Al alloy A356 poured at 685 °C.

Two casting methods were used—the first a more traditional method employing a direct gravity feed of the liquid metal into the mold of the blank cavity to form the specimen, allowing the liquid metal to flow down from the top leg to fill the other branching legs. The second approach used a counter-gravity method allowing the liquid metal to flow into the bottom leg and up into the branching legs under controlled flow conditions to minimize turbulence. Figure 1 shows photographs of a typical PLA blank with two specimens attached—an as-manufactured casting before specimen removal and removed specimens before being sectioned from their attachments to the horizontal arm from left to right, respectively. Specimens are then sectioned from their arm and further physically processed, that is, excess or unnecessary material is removed by sanding, filing, grinding, or other methods, if required. The blank can be placed in the casting flask before encapsulation by plaster in the direct gravity feed orientation shown in the left image of Fig. 1 or vertically flipped, which determines if the metal flow will be vertically going up by counter gravity method or down by direct gravity method into the specimens. In

fact, the blank was upside down relative to the left image in the casting flask in the middle image. It was flipped back over to show the specimens in the right image. This will be discussed in more detail in the section on the specimens themselves.

Fig. 1 Photographs of a PLA blank, finished casting, and removed specimens (from casting plaster)

3. XCT Scan Method

Aluminum is a relatively lower X-ray attenuating metal, unlike titanium, iron, steel, and even more attenuating metals, and can often be sufficiently penetrated by lower X-ray energies. This is especially true if the specimen (sample), part, or component can be oriented in the X-ray beam so as not to present any relatively long, very attenuating X-ray path lengths compared to a significant majority of short ones during a 360° rotation. This was accomplished with Al tetrahedral and octahedral specimens by stably resting them on three of their legs during scanning. In the case of tetrahedral specimens, this meant that one leg was vertical. In the case of octahedral specimens, this meant that the so-called front leg facing the X-ray source was slanted down with its end forming part of the base, while the opposite back leg facing the detector was slanted up. This prevented any path length from having to go through about two leg lengths of Al, which would have been a relatively long, asymmetric path length compared to the diameter of the legs. A 225-kVp variable focal spot size, microfocus X-ray tube was used to XCT scan the tetrahedral and octahedral specimens. Given the small size of the leg diameters, a little less than one-quarter inch, a relatively low X-ray voltage and thus energy, along with minimal tube current, was used to minimize the focal spot size or area of origin of the X-rays coming from the tube. Minimizing the focal spot size both minimizes

geometric unsharpness, or blurriness of edges, allowing greater geometric magnification and decreases or optimizes the effective pixel or voxel size. The magnification was chosen to both use the smallest field of view on the detector as possible, needing only a subset of its area for faster scanning (fewer projections), and to keep the unsharpness below 1 pixel, which is a standard practice in X-ray CT imaging. The combination of XCT parameters chosen resulted in a focal spot size of about 69 µm and an effective pixel pitch or size of 55 µm. All the basic parameters of the XCT technique used to scan the specimens are given in Table 1. The detector sampling rate of 12.08 frames per second (fps), which is relatively fast, was optimized in relation to the other parameters to minimize scan times while still providing enough X-ray response at the detector to produce very good XCT projection images, thus resulting in excellent XCT volume reconstructions.

Table 1 XCT scanning parameters

Parameter	Value
X-ray voltage (peak)	150 kV
X-ray energy (peak)	150 keV
X-ray current	530 µA
Detector sample rate	12.08 fps
X-ray focal spot size	69 µm
Source-to-image distance	595.45 mm
Source-to-object distance	163.50 mm
Magnification	3.64
Detector element pitch	200 µm
Effective pixel pitch	54.9 µm
Unsharpness	0.91 pixels
Frame average	4×
No. projections (views)	1800
Source filter	None
Detector filter	None

4. Specimen Descriptions

Two types of test specimens were designed, which were considered complex structures, including tetrahedral (four-legged) and octahedral (six-legged) “star” shaped structures. PLA blanks of the designs were fabricated using a fused deposition modeling (FDM) desktop 3-D printer. In addition, other PLA support structures and lids were fabricated to support the blanks during the molding process. Ideally, fabricated PLA blanks and their corresponding cast specimens should match with the “actual” 3-D CAD structure with zero surface deviation. Figure 2 shows the CAD-generated 3-D surface models (STL files) for both the tetrahedral and octahedral star specimens that were used for dimensional comparison. Both star

specimen designs had leg lengths of 30 mm (1.2 inches) with a diameter of 6 mm (0.24 inches). After fabrication of the PLA blanks, specimens were prepared prior to casting. All unwanted material was removed from the specimens, such as burs and any remains of leg support/backing.

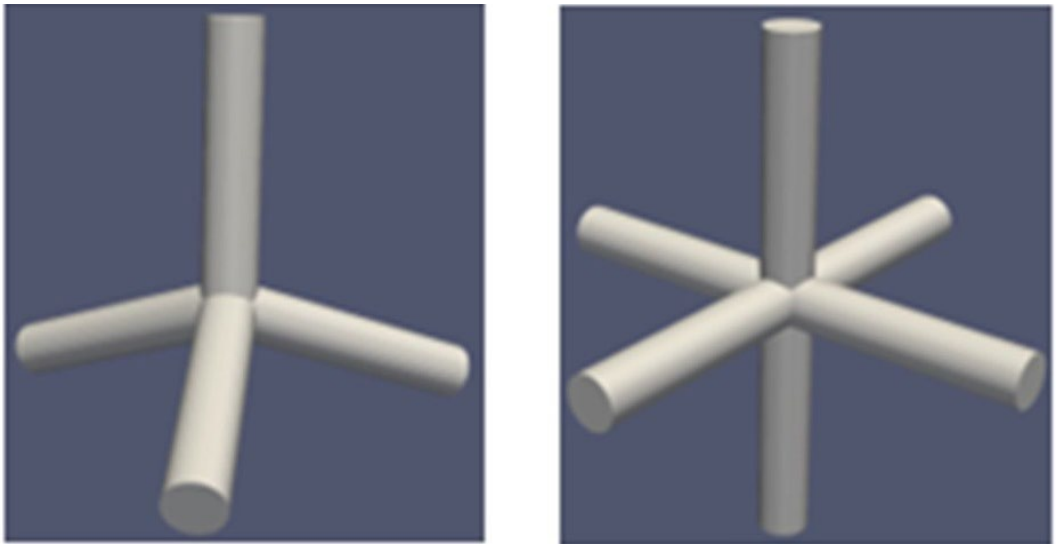

Fig. 2 Physical 3-D CAD star structure designs used for dimensional comparisons

In the first phase of the program, several tetrahedral and octahedral "star"-shaped Al specimens were fabricated in sets. The first set consisted of two tetrahedral specimens, named A and B, and the second set consisted of two tetrahedral specimens and one octahedral specimen. The first tetrahedral specimen in the second set was manufactured before the other two in the set, which were manufactured over the same period. Specimens A and B were manufactured with the PLA blank in the direct gravity feed orientation shown in the left image of Fig. 1, so the metal flow was down into the attached leg from above and spread into the other legs from there. On the other hand, all the specimens of the second set were manufactured with the blank vertically in the opposite direction in the counter gravity feed orientation, so the metal flow was up into the attached leg from below and spread into the other legs from there. The metal flow direction into all three specimens of the second set is shown in Fig. 3, in which the downward-pointing black-labeled legs were attached to the arm of the blank. The black, red, green, blue, and orange end labels were put on using colored markers and used as position indicators to correlate the XCT scan orientation to the casting process orientation.

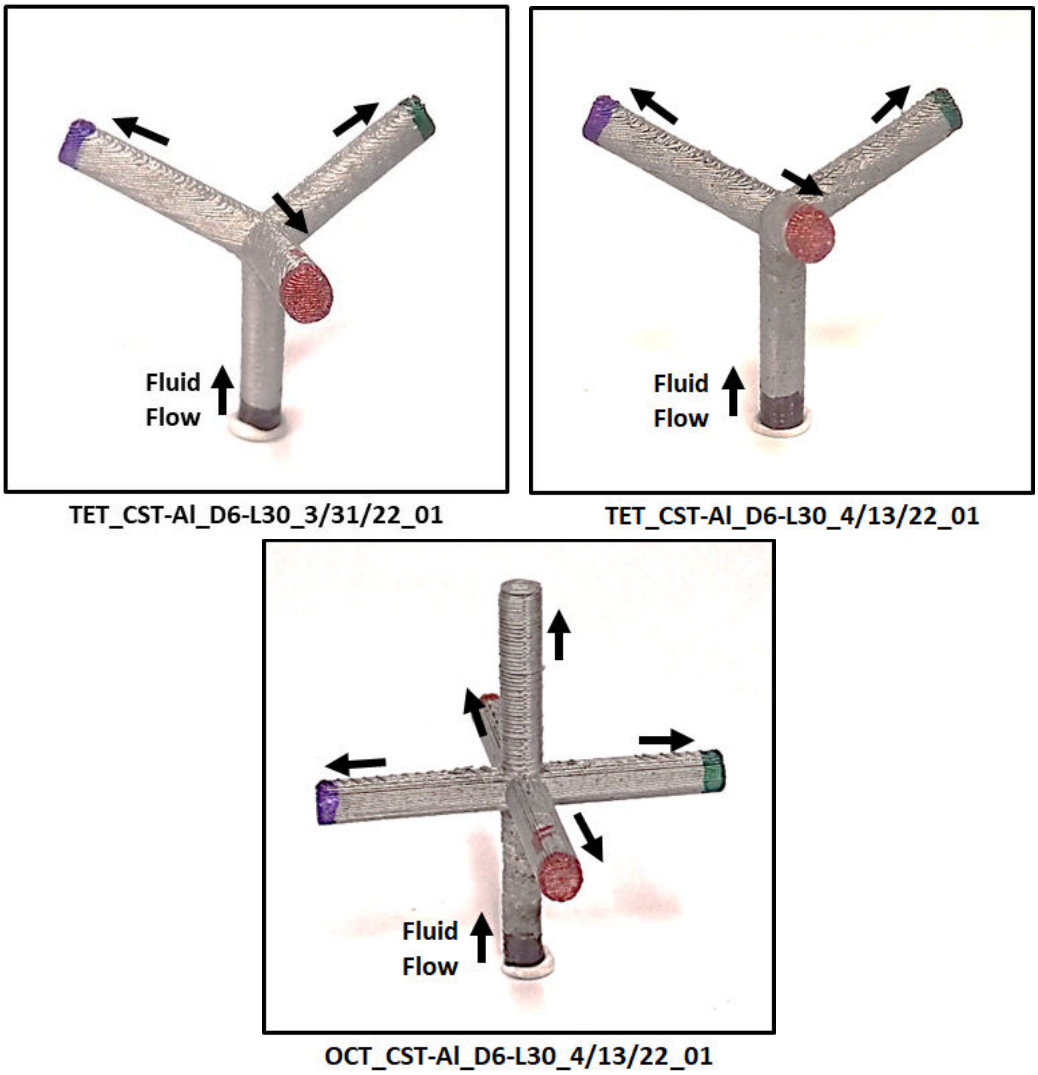

Fig. 3 Direction of molten metal flow in the specimens of the second set

Figure 4 shows a photograph of Specimen A from the first set with leg diameters and lengths of 6 mm (0.24 inches) and 30 mm (1.2 inches), respectively.

Fig. 4 Tetrahedral cast Al specimen

5. XCT Image Analysis Using Volume Graphics' Software

Reconstructed volumes from the XCT scans were imported into Volume Graphics' (VG) Studio MAX (VGSM) software for individual nominal-to-actual comparison and production of a surface STL model. Each volume was initially registered/reoriented to match the orientation it was scanned in. This way, the color labels on the legs of each specimen could be correlated and marked in the software. Following the registration, a surface determination was performed via segmentation of the volume gray-level histogram. VG's surface determination tool includes advanced filtering options, which were used to remove noise particles and small voids found in the data. This helps eliminate the presence of internal structures like pores or cracks and external "floating" particles from noise or stray particles imbedded in scanning mounting fixtures from the final surface data. Once finished, the corresponding CAD model for the specimen was also loaded into the VG scene. The model was then roughly registered to the same orientation as the sample volume, after which a Best-Fit registration was applied to further refine their alignment. At this point, the nominal-to-actual comparison was run to measure surface deviation between the sample volume and the model. The analysis produces a deviation histogram within a user-specified range and overlays a color-gradient "heat map" on the surface of the sample volume's 3-D rendering. The range of the histogram was tailored to better fit the bounds of the data, which also adjusted the rendered color map. The final processing step for each sample was to produce an STL mesh of the sample surface. Again, this was done in VG with the Export Mesh

module. There, the accuracy and number of vertices can be tailored to the user's needs.

6. XCT Results and Discussion

Figure 5 shows complete 3-D solid visualizations of Specimen A, of which the second and third images are virtually sectioned to show interior surfaces and features. The top-left image shows that the legs of Specimen A have a relatively uniform diameter and cylindrical shape. The top-right image has the forward-pointing leg removed and exhibits relatively small-sized internal porosity. The bottom image has the vertical leg removed and exhibits small-sized porosity in other legs. The presence and sizes of the porosity are not critical in these test specimens as they were fabricated to measure external dimensional accuracy.

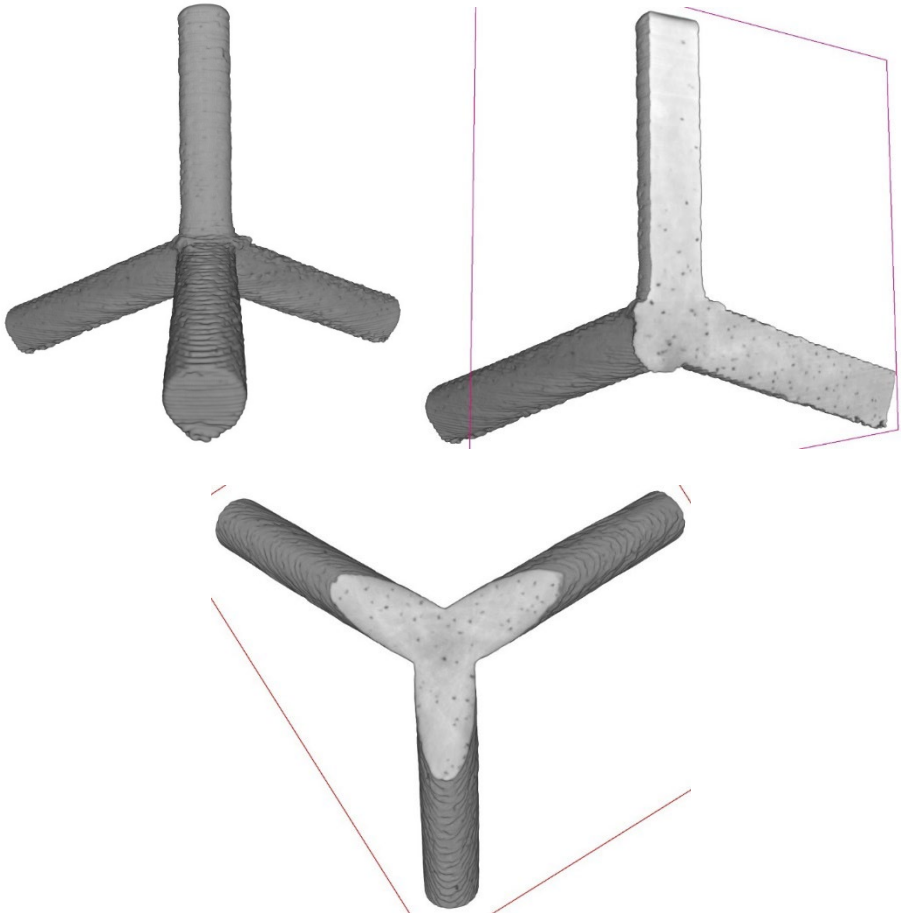

Fig. 5 Complete 3-D solid visualizations of Specimen A, of which the second and third images are virtually sectioned to show interior surfaces and features

Figure 6 shows complete 3-D solid visualizations of Specimen B, of which the second and third images are virtually sectioned to show interior surfaces and features. The top-left image shows that the legs of Specimen B have a smaller diameter than those of Specimen A and do not have a uniform diameter or cylindrical shape. The top-right image has the forward-pointing leg removed and exhibits extensive relatively large-sized internal porosity. The bottom image has the vertical leg removed and exhibits large-sized porosity in other legs. The relative lack of material in Specimen B may be due to a blockage that developed during the casting process or unsuccessful burnout in which PLA material remained in the casting and impeded metal flow.

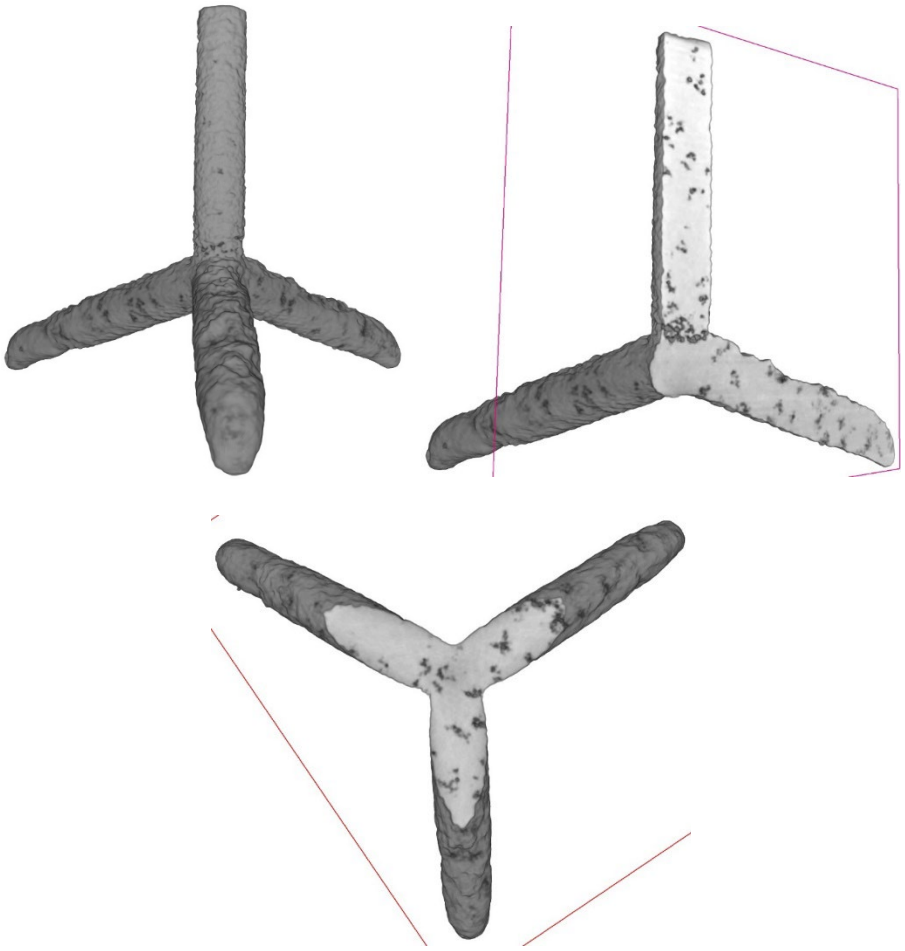

Fig. 6 Complete 3-D solid visualizations of Specimen B, of which the second and third images are virtually sectioned to show interior surfaces and features

Figure 7 shows a complete 3-D solid visualization of the outside surfaces of the first tetrahedral Al specimen of the second set (left) and a 2-D planar view exhibiting internal extended porosity and/or cracks in the red-labeled leg (right). The first tetrahedral specimen was manufactured by itself at an earlier date than the

other two in the second set. This was mainly due to wanting to see the casting result of the first specimen by itself. It is believed that the casting process of the first specimen proceeded as expected without difficulties, as was the case with the other two specimens in the set. Again, the presence and sizes of the porosity are not critical in these test specimens as they were fabricated to measure external dimensional accuracy. Figure 8 shows the nominal-to-actual comparison analysis of the tetrahedral specimen shown in Fig. 7 using VGSM software, which shows the color-coded difference between the model and actual surface displayed over the surface of the specimen and quantified by the scale (mm) on the left. Figure 9 shows the quantitative histogram of the differences in surface location between the model and the actual tetrahedral specimen. The x- and y-axes in the histogram are deviation distance (mm) and net surface area at that distance (mm^2), respectively.

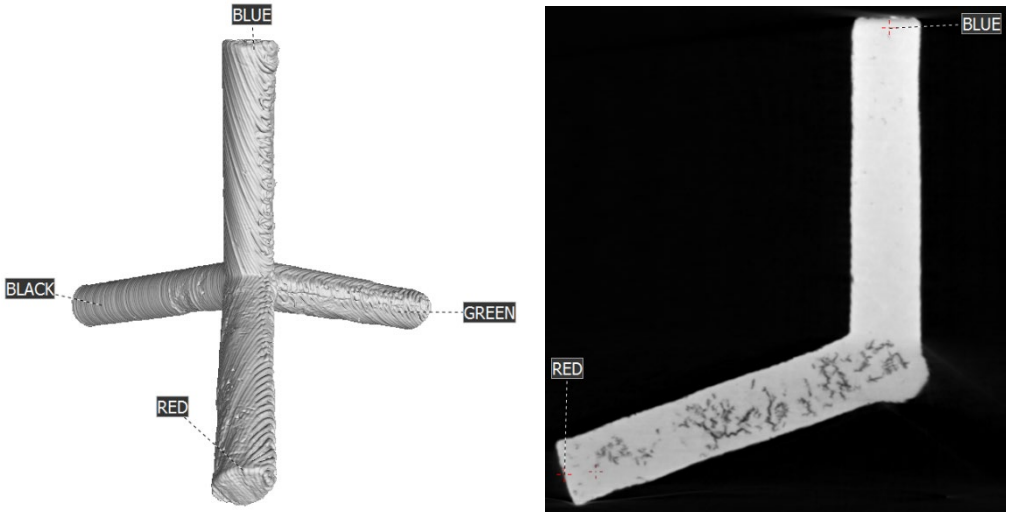

Fig. 7 3-D solid and 2-D planar images of first tetrahedral cast Al specimen in second set

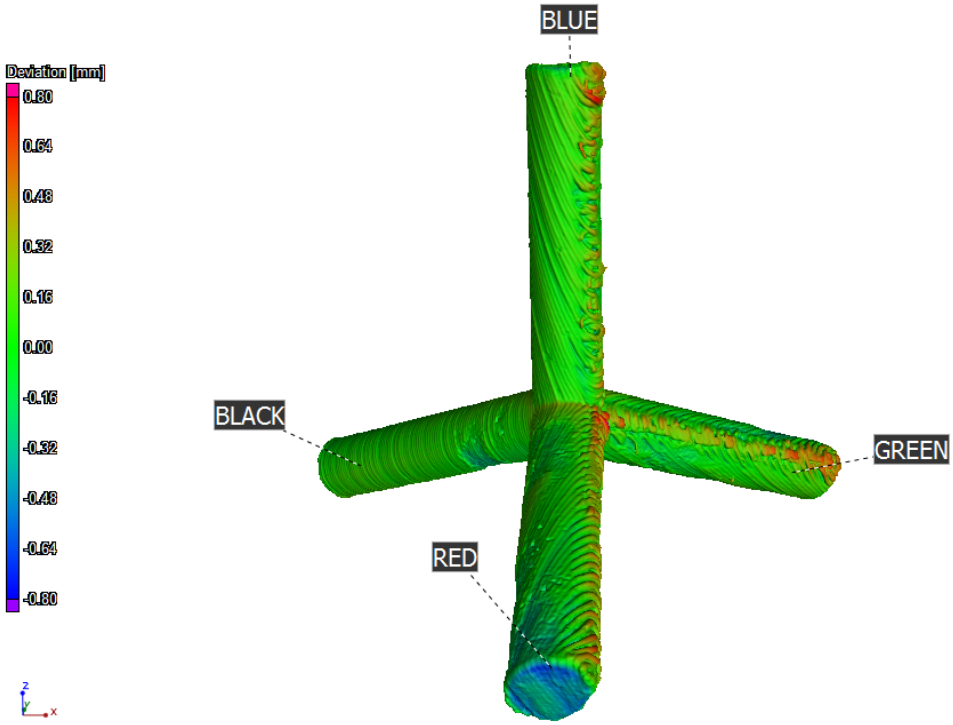

Fig. 8 Nominal-to-actual comparison analysis of first tetrahedral cast Al specimen in second set showing the color-coded deviation overlaid on the specimen surface and deviation scale (mm) on the right and left, respectively

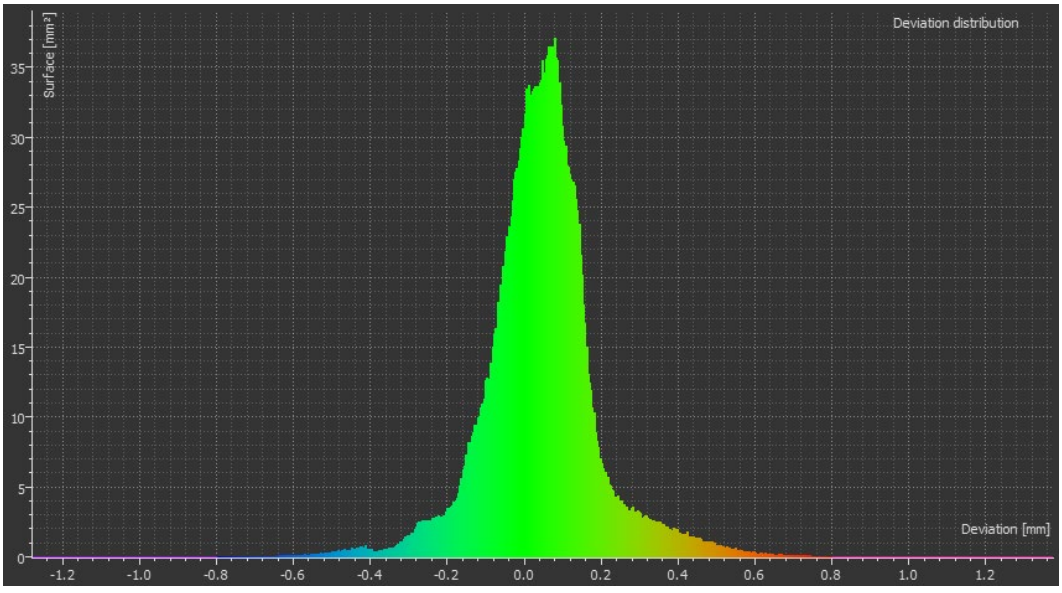

Fig. 9 Histogram of the differences in surface location between the model and actual surface of the first tetrahedral specimen in the second set, in which the x- and y-axes are deviation distance (mm) and net surface area at that distance (mm^2), respectively

First, it is readily apparent that the surface features of the specimens have been reliably reproduced given the pixel size and are clearly visible in the 3-D solid images in Figs. 5–8. The surface features are basically a result of the manufacturing casting process, except for Specimen B that had a cast processing problem. The end surface of the red-labeled leg of the specimen has areas with both a bluish and cyan hue in Fig. 8, which are negative deviations meaning that the specimen surface does not physically extend out to the model surface. There are also some faint bluish hues near the end of the red-labeled leg and on the black-labeled leg closer to the middle of the specimen on their circumferential surfaces. The deviation scale on the left goes from positive 0.80 mm (red) to negative 0.80 mm (blue) with zero deviation represented by a medium green color. Any deviation more than 0.80 mm on the positive or negative (i.e., –0.81-mm and less) side of the model is represented by pink and purple, respectively. The deviation histogram of the specimen in Fig. 9 essentially has a single-mode distribution centered slightly to the right of 0.00 mm at about 0.08 mm. The optimal distribution would have a single mode or peak with positive and negative deviations symmetrically distributed about 0.00 mm (zero deviation), as well as both minimal main peak width and shoulder and/or tail lengths. Of course, it is extremely likely that the surface of any manufactured specimen, part, or component will never exactly match the model, so there will always be a certain amount of deviation from it. There seems to be very little, if any, deviation beyond about 0.68 mm and –0.60 mm on the righthand and lefthand sides of the histogram, respectively. Hence, there are no pink or purple colors on the surface of the specimen in Fig. 8. A large majority of all deviations are between 0.20 and –0.20 mm with some shoulder distribution and relatively short tails on both sides of the histogram. The majority of the deviations are positive. The likely reason for the presence of most of the positive deviations in the histogram is that there are circumferential surface areas of the legs of the specimen that extend beyond the model surface, which are positive deviations, rather than deviations at the end surfaces of the legs. It is also likely that most of the negative deviations are due to a combination of differences at the end surfaces of legs and underfilled areas like those previously mentioned in the red- and black-labeled legs.

Figure 10 shows a complete 3-D solid visualization of the outside surfaces of the second tetrahedral Al specimen in the second set (left) and a 2-D planar view exhibiting internal porosity in two of the legs (right). Figure 11 shows the nominal-to-actual comparison analysis of the tetrahedral specimen shown in Fig. 10 using VGSM software, which shows the color-coded difference between the model and actual surface displayed over the surface of the specimen and quantified by the scale (mm) on the left. Figure 12 shows the quantitative histogram of the differences in surface location between the model and the actual tetrahedral

specimen. The x- and y-axes in the histogram are deviation distance (mm) and net surface area at that distance (mm^2), respectively.

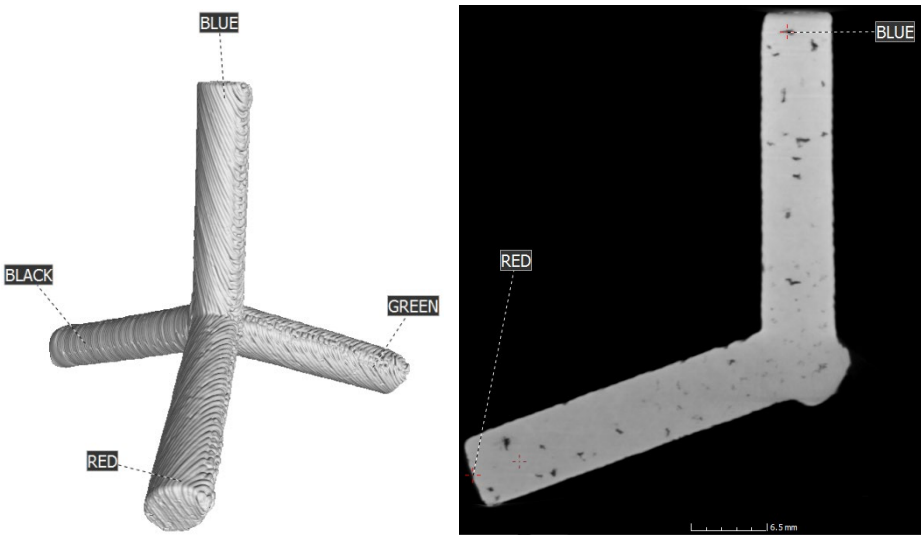

Fig. 10 3-D solid and 2-D planar images of second tetrahedral cast Al specimen in second set

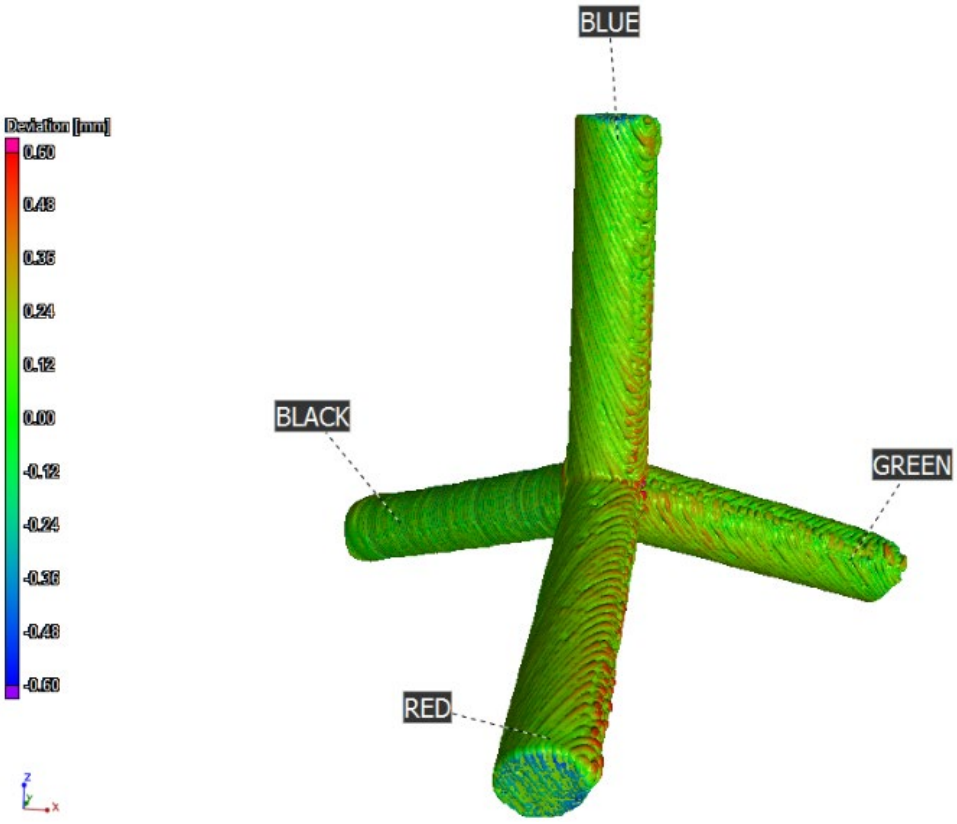

Fig. 11 Nominal-to-actual comparison analysis of second tetrahedral cast Al specimen in second set showing the color-coded deviation overlaid on the specimen surface and deviation scale (mm) on the right and left, respectively

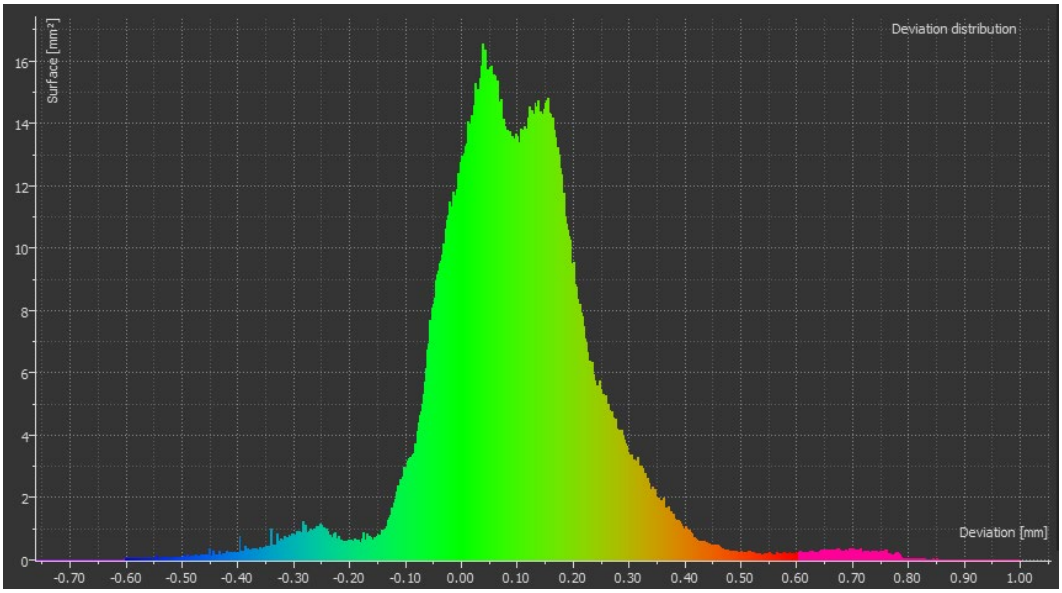

Fig. 12 Histogram of the differences in surface location between the model and actual surface of the second tetrahedral specimen in the second set, in which the x- and y-axes are deviation distance (mm) and net surface area at that distance (mm^2), respectively

Again, it is readily apparent that the surface features of the specimen have been reliably reproduced. The end surfaces of the red- and blue-labeled legs of the specimen have some areas with a bluish hue in Fig. 11, which are negative deviations meaning that the specimen surface does not physically extend out to the model surface. The deviation scale on the left goes from positive 0.60 mm (red) to negative 0.60 mm (blue) with zero deviation represented by a medium green color. Any deviation more than 0.60 mm on the positive or negative (i.e., –0.61 mm and less) side of the model is represented by pink and purple, respectively. The deviation histogram of the specimen in Fig. 12 has a main bimodal distribution, which is not optimal, as well as a relatively much-lower peak centered at about –0.25 mm. The higher peak of the bimodal pair is centered slightly to the right of zero deviation at about 0.05 mm. The lower peak of the pair is centered at about 0.15 mm. A large majority of all deviations are between 0.30 and –0.10 mm with minimal shoulder distribution and relatively long tails on both sides of the histogram, including the very-low peak on the lefthand side. A relatively very-large portion of the deviations are positive. The histogram is shifted from being centered around zero deviation, which is logical given the bimodal distribution with both peaks centered at positive deviations. Some of the most distended or farthest out bulbous or ridge-like surface features appear to have reddish hues, which are positive deviations. Lastly, there seems to be very little, if any, deviation beyond about –0.55 mm on the lefthand side of the histogram (no purple colors in Fig. 11), whereas a significant portion of the tail on the righthand side of the histogram is beyond 0.60 mm, which is pink colored. However, most, if not all, of the

circumferential surfaces of the legs of the specimen do not seem to have any pink colors on them in Fig. 11. The likely reason for the positive deviations in general, as well as the presence of the second lower bimodal peak, is that there are circumferential surface areas of the legs of the specimen that extend beyond the model surface, which are positive deviations, rather than deviations at the end surfaces of the legs. It is also likely that most of the tails on both sides of the histogram are due to deviations at or very near the end surfaces of the legs.

Figure 13 shows a complete 3-D solid visualization of the outside surfaces of the octahedral Al specimen (left) and a 2-D planar view exhibiting internal extended porosity and/or cracks in multiple legs (right). Figure 14 shows the nominal-to-actual comparison analysis of the octahedral specimen shown in Fig. 13 using VGSM software, which again shows the color-coded difference between the model and actual surface displayed over the surface of the specimen and quantified by the scale (mm) on the left. Figure 15 shows the quantitative histogram of the differences in surface location between the model and the actual octahedral specimen.

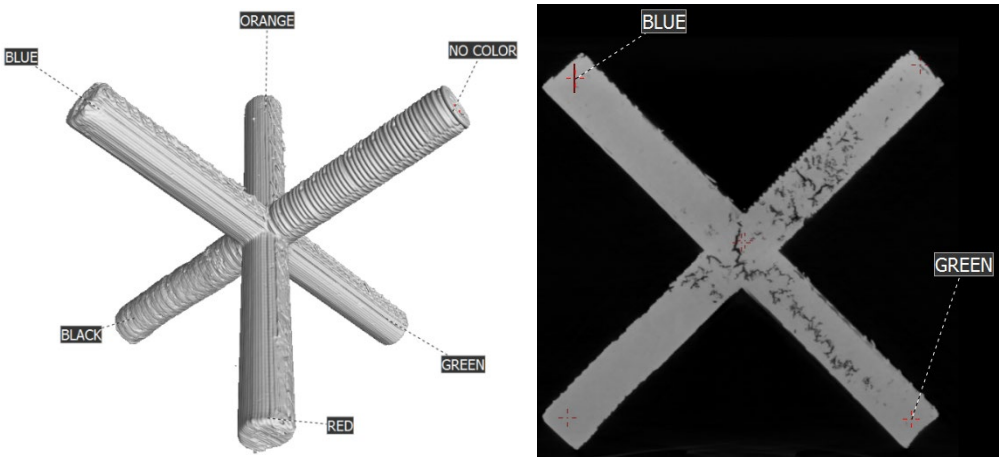

Fig. 13 3-D solid and 2-D planar images of the octahedral cast Al specimen

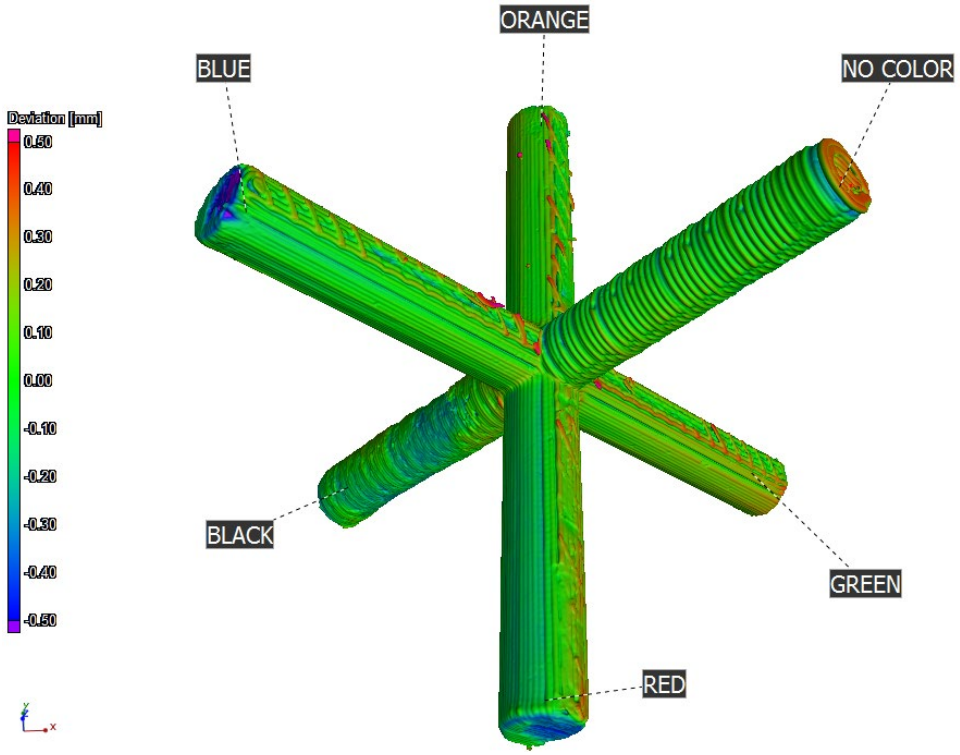

Fig. 14 Nominal-to-actual comparison analysis of the octahedral cast Al specimen showing the color-coded deviation overlaid on the specimen surface and deviation scale (mm) on the right and left, respectively

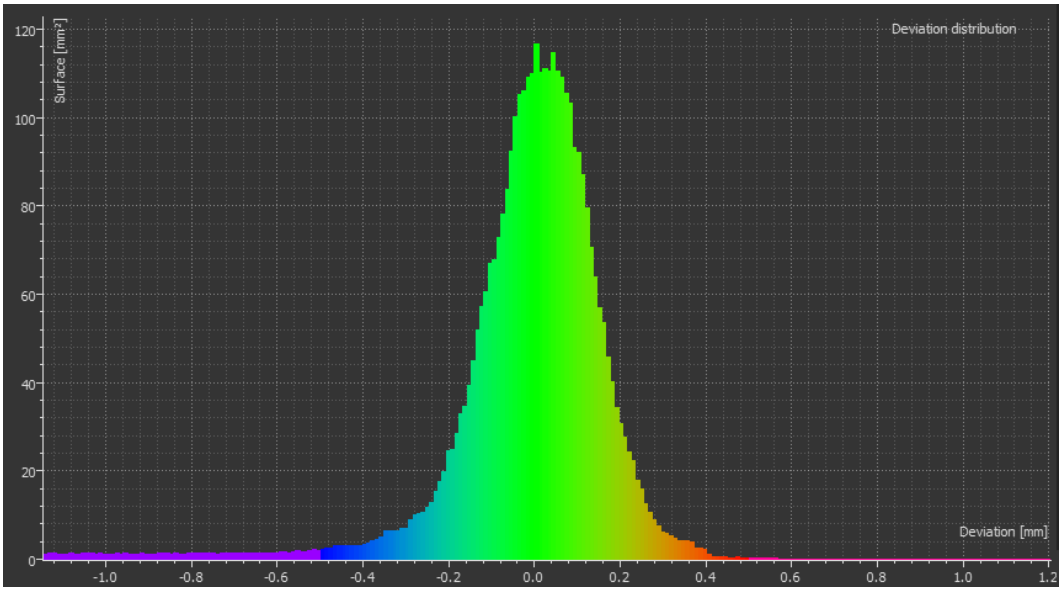

Fig. 15 Histogram of the differences in surface location between the model and actual surface of the octahedral specimen, in which the x- and y-axes are deviation distance (mm) and net surface area at that distance (mm^2), respectively

It is readily apparent that the surface features of the specimen have been reliably reproduced. The end surfaces of the red- and blue-labeled legs of the specimen have some areas with a dark bluish hue in Fig. 14, which again are negative deviations, as well as areas with a light bluish hue on the middle and lower circumferential surface of the black-labeled leg. Some of the legs also appear to have long bluish lines along their length or bluish circumferential rings, which are negative deviations. These features may be present due to surface characteristics of the PLA blank being transferred to the cast specimen. Also, the "NO COLOR" labeled leg has areas with a reddish hue on its end surface. The deviation scale on the left goes from positive 0.50 mm (red) to negative 0.50 mm (blue) with zero deviation represented by a medium green color. Any deviation more than 0.50 mm on the positive or negative (i.e., –0.51 mm and less) side of the model is represented by pink and purple, respectively. The deviation histogram of the octahedral specimen in Fig. 15 has a single-mode distribution centered very close to 0.00 mm, which is optimal, unlike the second tetrahedral specimen. A large majority of all deviations are between 0.20 and –0.20 mm with minimal shoulder distribution and very little tail on the righthand side of the histogram. The main peak is also basically symmetric about the zero deviation. A slight majority of the deviations may be positive. The tail on the righthand side of the histogram is very short with no deviations beyond about 0.52 mm (no pink colors in Fig. 14), whereas the tail on the lefthand side is very long and extends out to about –1.14 mm with much of it colored purple. Positive deviations like those at the end surface of the NO COLOR leg probably make up very little of the tail on the righthand side of the histogram. However, the very-long tail on the lefthand side with the substantial purple section is likely made up of a combination of both negative deviations at the end surfaces of multiple legs and the previously mentioned blue-hued line and ring deviations.

Figure 16 is a photograph of the jointed section of the octahedral specimen showing a sizeable surface crack. The right image of Fig. 13, which is sectioned through about the center axes of the legs, shows this crack internally going vertically right through the center of the jointed region with it spanning almost the entire region.

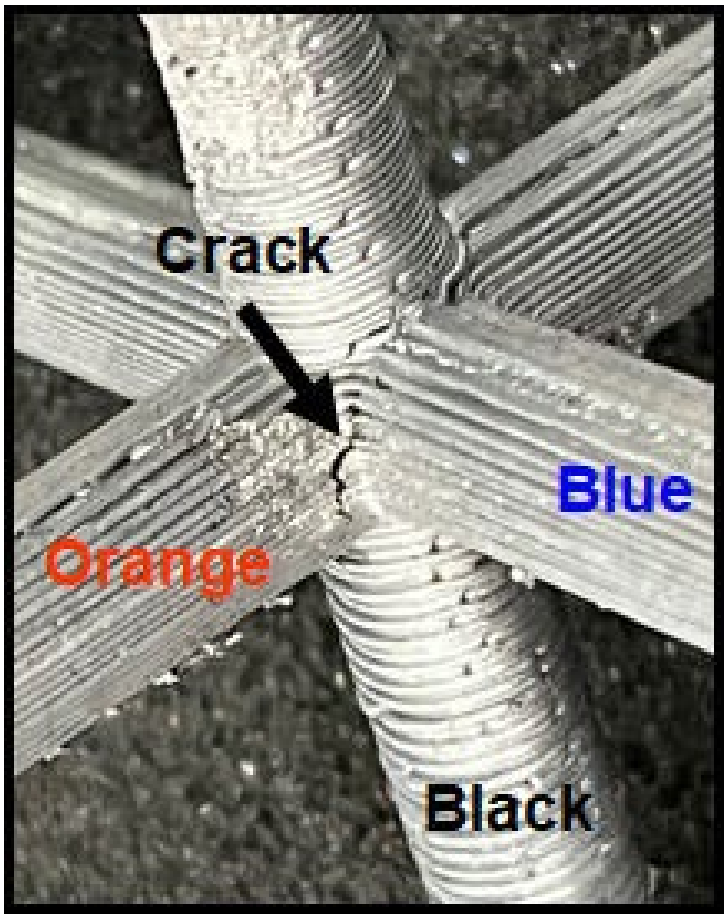

Fig. 16 Sizeable crack in the outside surface of the joint region of the octahedral Al specimen

7. Summary and Conclusions

The overall purpose of the ARL Advanced Manufacturing Co-Design Program is to develop and test novel AM and casting methods for near-net or net-shape production of metallic components. The first casted set of specimens resulted in a relatively good Specimen A, and poor Specimen B, which suffered some sort of failed metal flow. The direction of the metal flow into the PLA blank was reversed in the second set of specimens, which may have prevented similar flow problems as Specimen B had in the set. Most of the negative deviations between the tetrahedral specimens in the second set and their surface models were likely from differences in the end surfaces of their legs. The octahedral specimen also had negative end-surface deviations as well as some negative linear and circumferential ring deviations in the main bodies of its legs. The majority of the deviations in the two tetrahedral specimens were positive with the second specimen having a large difference between positive and negative deviations. The distribution between positive and negative deviations in the octahedral specimen was appreciably closer.

The deviation histogram of the first tetrahedral specimen had a single-mode, or one peak, distribution centered slightly to the right of 0.00 mm at about 0.08 mm with some shoulder distribution and relatively short tails on both sides of the histogram. The likely reason for the presence of most of the positive deviations in the histogram is that there are circumferential surface areas of the legs of the specimen that extend beyond the model surface, which are positive deviations, rather than deviations at the end surfaces of the legs. The second tetrahedral specimen seemed to have a relatively small, consistently positive deviation in the main bodies of at least some of its legs, given its main bimodal or two-peak histogram. Its histogram was shifted to the positive righthand side due to the bimodal peaks and had minimal shoulder distribution and relatively long tails on both sides of the histogram. It also appeared to have larger positive deviations at some of its most distended or farthest out bulbous or ridge-like surface features. The octahedral specimen had a single-mode histogram centered at about zero deviation (0.00 mm) with a mostly symmetric distribution around it, unlike the second tetrahedral specimen. Its histogram had minimal shoulder distribution and a very-short tail on the righthand side, whereas the tail on the lefthand side was very long. Again, the likely reason for the presence of most of the positive deviations in the histogram is that there are circumferential surface areas of the specimen's legs that extend beyond the model surface rather than deviations at the end surfaces of the legs. The octahedral specimen also had a surface crack in its joint region that went deep into its interior.

It is believed that no detrimental casting process errors occurred during the manufacture of the second set of specimens. The presence of their surface features is normal for the current state of production. Hence, the deviation between the actual specimen surfaces and their surface models is mostly due to expected variability in their current manufacturing process and not errors or miscues. The XCT and nominal-to-actual comparison analysis results for the cast Al tetrahedral and octahedral specimens described in this report show how the program is using novel AM and casting processes to produce dimensionally near-net shape objects or components. Manufacturing approaches developed and tested in the co-design program will be applied to the production of important, specific Army-relevant parts and components.

8. References

1. ASTM E 1570-95a. Standard practice for computed tomographic (CT) examination. American Society for Testing and Materials; 1995.
2. Dennis MJ. Industrial computed tomography: nondestructive evaluation and quality control. In: Ahmad A, Bond LJ, editors. ASM Handbook. Vol. 17. American Society for Metals (ASM) International; 1989.
3. Newton TH, Potts DG, editors. Technical aspects of computed tomography. In: Radiology of the skull and brain. Vol. 5. The CV Mosby Company; 1981.
4. Stanley JH. Physical and mathematical basis of CT imaging. American Society for Testing and Materials (ASTM); 1986. ASTM CT Standardization Committee (E7.01.07), ASTM Tutorial: Section 3.

List of Symbols, Abbreviations, and Acronyms

2-D	two-dimensional
3-D	three-dimensional
Al	aluminum
AM	additive manufacturing
ARD	Army Research Directorate
ARL	Army Research Laboratory
CAD	computer-aided design
CT	computed tomography
DEVCOM	US Army Combat Capabilities Development Command
FDM	fused deposition modeling
fps	frames per second
ML	machine learning
PLA	polylactic acid
STL	stereolithography
VG	Volume Graphics
VGSM	VG Studio MAX
XCT	X-ray computed tomography

1 (PDF)	DEFENSE TECHNICAL INFORMATION CTR DTIC OCA
1 (PDF)	DEVCOM ARL FCDD RLD DCI TECH LIB
5 (PDF)	DEVCOM ARL FCDD RLW MB B LOVE W GREEN K KLAFF FCDD RLW MC C PERGANTIS FCDD RLW MF T CAIN